

Expediting Polysulfide Anchoring by Fe_3O_4 /Reduced Graphene Oxide Composite for High-Performance Lithium-Sulfur Batteries

Tanwir Ansari,^[a, b] Anamika Ghosh,^[a] Dipsikha Ganguly,^[a] Balasubramanian Muthiah,^[b] and Ramaprabhu Sundara^{*[a]}

The inherent low conductivity of sulfur, sluggish redox kinetics, and the challenge of maximizing active material utilization are the bottlenecks for practical implementation in lithium-sulfur (Li–S) battery technology. Herein, a low-cost Fe_3O_4 -rGO that serves as both a sulfur host matrix and an electrocatalytic interlayer in a Li–S battery has been synthesized. With the merit of high specific surface area, Fe_3O_4 -rGO offers high sulfur loading (80 wt.%) and sufficient space to accommodate sulfur volume expansion during the redox reaction. The symmetric cell experiment demonstrated that Fe_3O_4 in the rGO structure promotes the lithium polysulfide (LPS) redox conversion. The

Li–S battery is constructed using the Fe_3O_4 -rGO@S as the cathode and Fe_3O_4 -rGO as the interlayer, demonstrating an impressive specific capacity of 1258 $\text{mA}\text{h g}^{-1}$ at 0.1 C and the battery retained 76% of its capacity after 400 cycles at 0.5 C. This study also explores the confinement of LPS on the Fe_3O_4 -rGO@S– Fe_3O_4 -rGO cathode and interfacial redox kinetics by dynamic electrochemical impedance spectroscopy. This work presents a cost-effective method for improving the catalytic conversion of lithium polysulfides, which can contribute to the development of high-performance lithium-sulfur batteries.

1. Introduction

Impending climate change and growing energy demand prompted by population and economic growth create concern about environmental pollution associated with fossil fuel usage, which spurred the research on more advanced energy storage devices.^[1,2] Rechargeable Li–S batteries are emerging as highly promising candidates for future electrochemical energy storage solutions owing to their high theoretical specific capacity of 1675 $\text{mA}\text{h g}^{-1}$ and specific energy density of 2600 Wh kg^{-1} , which exceed the capacity of the conventional lithium-ion battery at a much lower cost. This higher capacity is attained from the conversion reaction in that sulfur is reduced to form polysulfide by reacting with lithium and forming Li_2S at the end of discharge.^[3–5] Furthermore, sulfur is plentiful and environmentally friendly, which renders Li–S batteries as a desirable and cost-efficient energy storage technology.^[6] In addition to the benefits, several intractable difficulties limit the practical use of Li–S batteries, which are associated with chemical reactions occurring at sulfur cathode and lithium anode. First, the low conductivity of sulfur ($\sim 10^{-30} \text{ S cm}^{-1}$) and its end

discharge product lithium sulfide ($\sim 10^{-13} \text{ S cm}^{-1}$) inhibit the electron transport in the sulfur electrode and hinder the electrochemical reaction kinetics.^[7] Second, the large volume expansion of sulfur (~80%) upon full lithiation from sulfur (S_8) to lithium sulfide (Li_2S) because of density disparity (2.03 vs. 1.66 g cm^{-3}) throughout the discharge process causes electrode damage and detachment from the current collector.^[8] Third, during the cyclic process of S_8 to Li_2S , higher-order polysulfide easily dissolves into the electrolyte, resulting in continuous accumulation of lithium polysulfide (LPS) and diffuses towards lithium anode driven by the concentration gradient where it reduces the chain length shuttle and re-shuttles towards the cathode. This phenomenon is referred to as the shuttle effect. As a result, Li–S batteries experienced rapid capacity degradation, poor coulombic efficiency during cycling, and have short cycle life.^[9,10] In order to overcome the aforementioned challenge strenuous efforts have been made by tailoring cathode materials. Carbon materials are extensively applied because of their sustainability and widespread availability.^[11,12] Combining sulfur with carbon-based materials, such as graphene,^[13] carbon nanotubes,^[14] porous carbons,^[15–17] nanofiber^[18] has been utilized in pursuit of enhancing electrical conductivity and promoting physical adsorption to dissolved polysulfide, rendering them superior host materials for encapsulating or loading sulfur to form a superior cathode. However, carbon materials depend solely on van der Waals interaction and endow limited sites available to adsorb polar polysulfide in the electrolyte. As a result, dissolution is not completely inhibited, causing inevitable capacity decay after prolonged cycling.^[19] Recently, it has been reported that polar metallic compounds, including TiO_2 ,^[20] TiO ,^[21,22] MnO_2 ,^[23,24] NiS_2 ,^[25] V_2O_5 ,^[26] and Ti_4O_7 ,^[27] could form strong chemical interaction

[a] T. Ansari, A. Ghosh, D. Ganguly, Prof. R. Sundara

Alternative Energy and Nanotechnology Laboratory (AENL), Nano Functional Materials Technology Centre (NFMTC), Department of Physics, Indian Institute of Technology Madras, Chennai 600036, India

E-mail: ramp@iitm.ac.in

[b] T. Ansari, B. Muthiah

Ceramics and Composites Laboratory, Department of Metallurgical and Materials Engineering, Indian Institute of Technology Madras, Chennai 600036, India

 Supporting information for this article is available on the WWW under <https://doi.org/10.1002/batt.202400716>

towards lithium polysulfide. Nonetheless, many polar metallic compounds exhibit poor electrical conductivity, which hinders fast electron transport and consequently reduces the rate capability.^[28] Additionally, polar materials constrain the LPS immobilization approach due to their slow redox kinetics in converting LPS to the end discharge product, Li₂S. This causes uncontrollable Li₂S deposition and flooding of LPS on the cathode due to the high activation energy required for further oxidation of Li₂S, and its poor conductivity slows down the conversion. This flooding causes the diffusion species to move towards the anode driven by the potential gradient.^[29] In this context, enhancing conversion kinetics between LPS and end discharge product, inhibiting dissolution and diffusion kinetics is the potential strategy to inhibit the shuttle mechanism in order to achieve the high-energy lithium-sulfur battery.

Iron-based materials have been extensively studied in the catalysis field due to their widespread availability, cost-effectiveness, and natural catalytic activity. Recently, DFT calculations showed that the chemical interaction between Fe₃O₄ and polysulfide possesses strong polar-polar interaction.^[30] Fe₃O₄, as a polar material, demonstrates robust chemical interactions with polysulfides and exhibits superior electrical conductivity (5×10^4 S m⁻¹) compared to other metal oxides.^[31] In this regard, Fe₃O₄ has been investigated as a sulfur host and interlayer material. Lu et al. have shown that a carbon cloth composite with strongly interconnected Fe₃O₄ and nitrogen-doped carbon can achieve a high sulfur loading and impressive capacity, serving as an effective cathode.^[32] In another study demonstrated by Liu et al. that a Li-S battery with a sulfur cathode configuration results in a capacity of 589 mAh g⁻¹ at a 2 C rate after the incorporation of a multifunctional Fe₃O₄-rGO interlayer.^[33] Inserting a conductive interlayer between the cathode and separator effectively inhibits the migration of LPS,

improves the utilization of active material, and acts as an upper current collector.

Based on the above understanding, the electrocatalytic interlayer Fe₃O₄-rGO and Fe₃O₄ coated on a glass microfibre separator act as an upper current collector and confine lithium polysulfide effectively. Herein, a simple procedure has been used to synthesize Fe₃O₄-rGO composite, which is employed as a sulfur scaffold and that supports high sulfur content and is effective in buffering the volume expansion. Fe₃O₄-rGO@S cathode shows low specific capacity with glass microfibre separator, which results in inefficient use of active materials. Hence, in this study, the Li-S battery is constructed with Fe₃O₄-rGO@S cathode and Fe₃O₄-rGO and Fe₃O₄ as interlayers. With this advantage, the Fe₃O₄-rGO interlayer exhibits a large initial discharge capacity of 1258 mAh g⁻¹ at 0.1 C rate and a low capacity decay rate of 0.049% per cycle up to 400 cycles with coulombic efficiency close to ~99.2% at 1 C. The enhanced performance of the Fe₃O₄-rGO interlayer can be attributed to the synergistic effect of Fe₃O₄ nanoparticles in conjunction with rGO. Dynamic Electrochemical Impedance Spectroscopy (DEIS) is used to evaluate the electrocatalytic information of the Fe₃O₄-rGO interlayer during the charge-discharge electrochemical kinetics process.

Experimental Section

Synthesis of Fe₃O₄ and Fe₃O₄-rGO

Graphene oxide (GO) was prepared using a modified Hummer's method by the oxidation of natural graphite powder (Figure S1). Fe₃O₄ decorated rGO was prepared by facile one-step pyrolysis method using GO and ferric nitrate as illustrated in Figure 1. GO and iron nitrate were taken in 1:1.5 ratio and ground using a

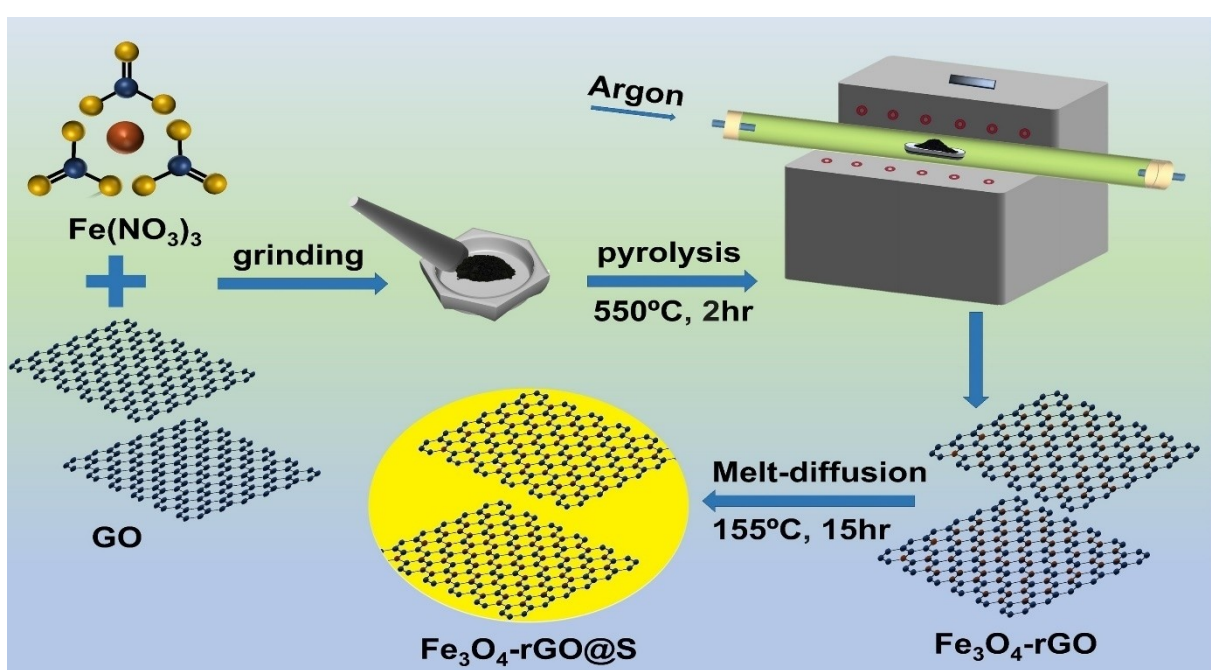


Figure 1. Synthesis of exfoliated Fe₃O₄-rGO.

mortar & pestle for uniform mixing. The powder was spread in a quartz boat, placed in the middle of the quartz tube, heated in an argon atmosphere in tubular furnace at 550 °C for 2 h and then the sample was collected for sulfur loading.

Synthesis of Fe_3O_4

Iron sulfate and iron nitrate were mixed in 50 mL deionized water in a 2:1 ratio, respectively. Ammonium hydroxide solution was added drop by drop to the as-prepared solution slowly with vigorous stirring. Then, the solution was transferred to a 100 mL Teflon-lined autoclave and stored at 130 °C for 3 h. The precipitate was collected, carefully washed with DI water, and dried at 60 °C.

Synthesis of Fe_3O_4 -rGO@S

Sulfur-impregnated Fe_3O_4 -rGO@S is achieved by melt diffusion method. The as-synthesized Fe_3O_4 -rGO and sublimed sulfur were combined in 1:4 ratio and thoroughly blended in an agate mortar for 1 h to achieve a homogenous mixture. After sealing the well-mixed sample in an ampoule, the furnace temperature was slowly increased to 155 °C and was held there for 15 h to complete sulfur diffusion. Later, the temperature was raised to 300 °C and it was held for 1 h to remove the surficial sulfur.

Material Characterization

The crystal structure was investigated using an X-ray Diffractometer (Aries Benchtop, Panalytical) with Cu-K α radiation with a nickel filter. The morphological features and elemental mapping were analyzed using field emission scanning electron microscopy (FESEM, INSPECT-F 50). Elemental analysis was also performed with the INSPECT-F 50 instrument. The transmission electron microscopic study was performed using Tecnai 20 TEM at 200 kV. The X-ray photoelectron spectroscopy was carried out employing a Specs X-ray photoelectron spectrometer equipped with an X-ray Mg K α source and a PHOIBOS 100MCD analyzer. Raman spectroscopy was carried in a Raman microscope (Renishaw) with a 532 nm laser. Brunauer-Emmett-Teller (BET) specific surface area of the sample was determined using the Micromeritics ASAP 2020 surface area and porosity analyzer.

Electrochemical Measurements

The electrode slurry was prepared by mixing Fe_3O_4 -rGO@S, PVDF, and acetylene black in the weight ratio of 80:10:10 with a suitable amount of N-methyl-2-pyrrolidone (NMP) as the solvent. Doctor blade technique was used to coat the slurry on the Aluminum foil and dried at 60 °C for 8 h. The dried electrode was punched into a disk of 12 mm diameter. The electrochemical performance of the Fe_3O_4 -rGO@S electrode was evaluated using a CR2032 coin cell in an argon-filled glove box (oxygen and water < 0.1 ppm) with lithium as the anode, and glass fiber (GF/C) as a separator. The electrolyte was prepared by adding 1 M bis(trifluoromethane)sulfonimide lithium salt (LiTFSI) in 1,3-dioxolane (DOL) and 1,2-dimethoxyethane (DME) (1:1 v/v) with 0.2 M LiNO₃ additive. The sulfur loading on the cathode is maintained within 1.8–2.2 mg cm⁻². The coin cells were constructed using Fe_3O_4 -rGO and Fe_3O_4 interlayers, as well as without an interlayer for comparison. The interlayers of Fe_3O_4 -rGO and Fe_3O_4 were fabricated through a process involving the mixing of PVDF in NMP solvent, followed by coating onto glass fiber. Following the coating process, the samples underwent drying at 80 °C overnight in a vacuum oven. The dried samples were cut into 19 mm disks and utilized as

interlayers. A Biologic VSP-300 electrochemical test station was employed to conduct the Dynamic electrochemical impedance spectroscopy (DEIS) and cyclic voltammetry (CV) experiments. Galvanostatic charge-discharges and cycle life tests were carried out employing the Biologic BCS-810 battery cycler. The galvanostatic charge-discharge and CV measurements were conducted within the potential range of 1.8–2.8 V (vs. Li/Li $^+$). The DEIS measurement was performed in the frequency range from 10 mHz to 1 MHz.

Lithium Polysulfide Adsorption Test

The adsorption test was conducted by preparing 0.5 M Li₂S₆ by chemically reacting sublimated sulfur and Li₂S in 5:1 molar ratio into 1,3-dioxolane (DOL) and 1,2-dimethoxyethane (DME) (equal volume ratio 1:1) under magnetic stirring for 70 h within the argon-filled glove box. To conduct the LPS adsorption test, the prepared 0.5 M Li₂S₆ solution was diluted by incorporating 10 μ L of Li₂S₆ in 4 mL of DOL and DME solvents in a 1:1 volume ratio. 10 mg of Fe_3O_4 -rGO, Fe_3O_4 samples were added to the diluted solution and allowed to rest for 8 h. Using a Cary 100 UV-vis spectrophotometer from Agilent Technologies, the supernatant from the samples was examined under UV-vis radiation.

Symmetric Cells Fabrication for CV Analysis

For symmetric cell fabrication, Fe_3O_4 -rGO and Fe_3O_4 were ground with PVDF and acetylene black in the weight ratio of 8:1:1 in NMP solvent. The well-mixed slurry was coated using the doctor blade technique on the aluminum foil and dried at 70 °C for 10 h inside a vacuum oven. The active material was cut into a 12 mm circular disk. The electrodes were assembled inside the glove box into a CR2032 coin cell with glass fiber as a separator. The 0.2 M Li₂S₆ and 1 M LiTFSI in DOL and DME (1:1 v/v) was employed as electrolyte. The voltage range of CV measurement was -1 to 1 V (vs. Li/Li $^+$). The Li₂S₆ free electrolyte was also tested for reference.

Li₂S Deposition Test

The catholyte solution of Li₂S₈ (0.2 M) was prepared by dissolving lithium sulfide (Li₂S) and sulfur (S) in a 1:7 molar ratio in a tetraglyme solution containing 1.0 mol L⁻¹ LiTFSI. The mixture was stirred overnight at 60 °C to ensure complete dissolution. The Fe_3O_4 -rGO and Fe_3O_4 electrodes were prepared by mixing each material with PVDF in a 90:10 weight ratio, using NMP as the solvent. The as-prepared slurry was coated onto carbon paper, dried in a vacuum oven at 60 °C, and stored overnight. The electrodes were then cut into discs with a diameter of 16 mm to serve as the cathode. For coin cell assembly, 20 μ L of Li₂S₈ catholyte was applied to the cathode side, while 20 μ L of the electrolyte without Li₂S₈ was added to the anode side as the anolyte, glass fiber membrane was used as the separator. The batteries were initially discharged galvanostatically to 2.06 V at a current of 0.112 mA, followed by a potentiostatic discharge at 2.05 V.

2. Results & Discussion

The synthesis of Fe_3O_4 -rGO is schematically illustrated in Figure 1. The detailed synthesis mechanism has been previously described in the literature.^[34] Briefly, a mixture of GO and iron nitrate was heated from room temperature to 550 °C in an

argon atmosphere, leading to the thermal exfoliation of GO and the formation of Fe_3O_4 -rGO.

The diffraction pattern of Fe_3O_4 -rGO@S (Figure 2 (a)) reveals the successful integration of sulfur into the Fe_3O_4 -rGO structure without any phase transformation of the Fe_3O_4 -rGO structure. Additionally, sulfur also retains its structure as seen from the XRD pattern of Fe_3O_4 -rGO@S and sublimed S. For the Fe_3O_4 -rGO pattern, an additional carbon peak in the range of 24–28° is observed and that can be attributed to the diffraction peak of stacked rGO. The diffraction peak for Fe_3O_4 -rGO, at 2 θ values of 30.55, 34.80, 43.53, 57.19, and 62.94° correspond to (022), (113), (004), (115), and (044) planes, respectively indicating the cubic spinel structure (JCPDS card no: 011-1282). Raman spectroscopy is widely used and provides valuable insights into the structural features and composition of the samples. The Raman spectrum of Fe_3O_4 -rGO is shown in Figure 2 (b), which displays two prominent bands around 1342 cm^{-1} and 1598 cm^{-1} , corresponding to the D and G bands, respectively, along with additional bands appearing at 285 cm^{-1} and 603 cm^{-1} . The bands observed at 285 cm^{-1} and 603 cm^{-1} are attributed to the Fe–O vibrational modes, E_g and A_{1g} of Fe_3O_4 , respectively. They indicate the presence of Fe_3O_4 on the surface of the reduced graphene oxide surface.^[35]

The FESEM microstructure of the as-prepared sample is shown in Figure 3. Fe_3O_4 -rGO, depicting a sheet-like morphology of rGO along with uniformly distributed Fe_3O_4 nanoparticles is shown in Figure 3 (a, b). The distribution of Fe, C, and O is confirmed by EDS mapping (Figure S2 (a)). The Figures 3 (c, d), typical FESEM images of Fe_3O_4 -rGO@S, show that sulfur is uniformly dispersed in the Fe_3O_4 -rGO network. The uniformly distributed rGO network could improve the stability by buffering the volume changes within the cathode. The uniform distribution of S in Fe_3O_4 -rGO can be found from the EDS elemental mapping. The elements C, Fe, O, and S can be observed without impurity in Figure S2 (b). The Fe_3O_4 , as synthesized by the solvothermal method, shows spherical morphology with agglomerated particles and a narrow size distribution of particles (Figure 3 (e, f)). The corresponding elemental mapping is shown in Figure S2 (c). The TEM images,

as shown in Figures 3 (g, h and i) further demonstrate that the as-synthesized Fe_3O_4 -rGO has a uniform morphology, and Fe_3O_4 is homogeneously attached to the surface of rGO. Microscopic images reveal that the Fe_3O_4 particle is nearly spherical in shape on the rGO sheet. These spherical particles potentially disrupt the planar structure of rGO and contribute to increased defect densities. The HRTEM image indicates that the lattice distance of 0.25 nm corresponds to the (113) plane of Fe_3O_4 , which implies the crystallinity of the Fe_3O_4 material.

Thermogravimetric analysis (TGA) was performed on the as-synthesized Fe_3O_4 -rGO@S in an argon atmosphere to determine the content of sulfur and is shown in Figure S3. The volatilization of sublimed sulfur causes rapid mass loss at 150–350 °C, and the specific sulfur content is found to be 80 wt.%. X-ray photoelectron spectroscopy (XPS) was performed to better understand the surface chemistry and bonding states of the Fe_3O_4 -rGO@S sample. The survey spectrum of C 1s, O 1s, Fe 2p, and S 2p, as shown in Figure 4 (a), confirms the presence of C, O, Fe, and S elements in the materials. Figure 4 (b) shows the high-resolution C 1s spectrum, which can be deconvoluted into two sub-peaks positioned at 284.6 eV and 286.3 eV and that correspond to bonds of C–C and C–O, respectively.^[36] The high-resolution peaks observed at 162.7 eV and 163.6 eV correspond to the S 2p_{3/2} and S 2p_{1/2} states of S, revealing S²⁻.^[37] In addition, peak at 164.7 eV suggesting the possible existence of C–S bonds.^[38] Peaks at 168.8 eV originate from sulfate species from oxygen-oxidized sulfur after the deposition of sulfur in the presence of air, as shown in Figure 4 (c).^[39] In the high-resolution spectra, as shown in Figure 4 (d), the two peaks located at 711.4 eV and 724.5 eV can be attributed to Fe 2p_{3/2} and Fe 2p_{1/2} binding energy, respectively. The satellite peak at 719.6 eV shows the existence of Fe³⁺ in the Fe_3O_4 . Moreover, the appearance of the Fe–S signal at 707.9 eV was also identified.^[40,41] The fitted peak at 531.8 eV is for O 1s from the surface oxygen (Figure 4 e).

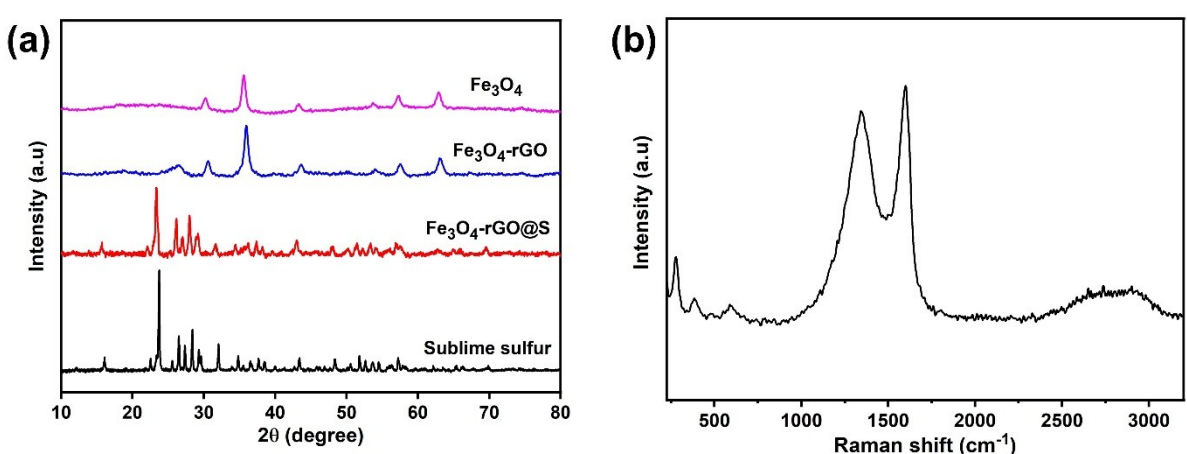


Figure 2. (a) XRD patterns of sublimed sulfur, Fe_3O_4 -rGO@S, Fe_3O_4 -rGO and Fe_3O_4 ; (b) Raman Spectrum of Fe_3O_4 -rGO.

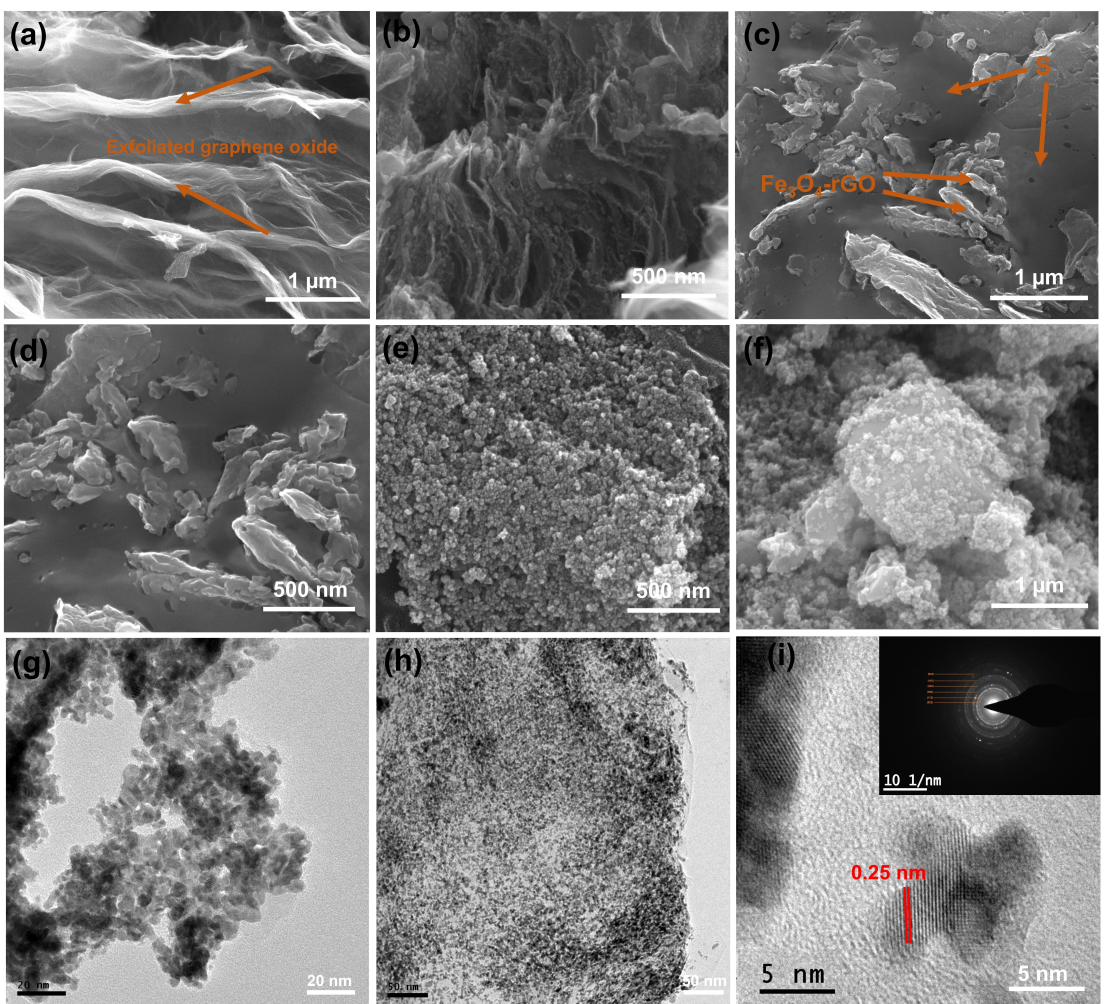


Figure 3. SEM images of Fe₃O₄-rGO (a, b); Fe₃O₄-rGO@S (c, d) and Fe₃O₄ (e, f); TEM images of Fe₃O₄-rGO sample (g, h and i).

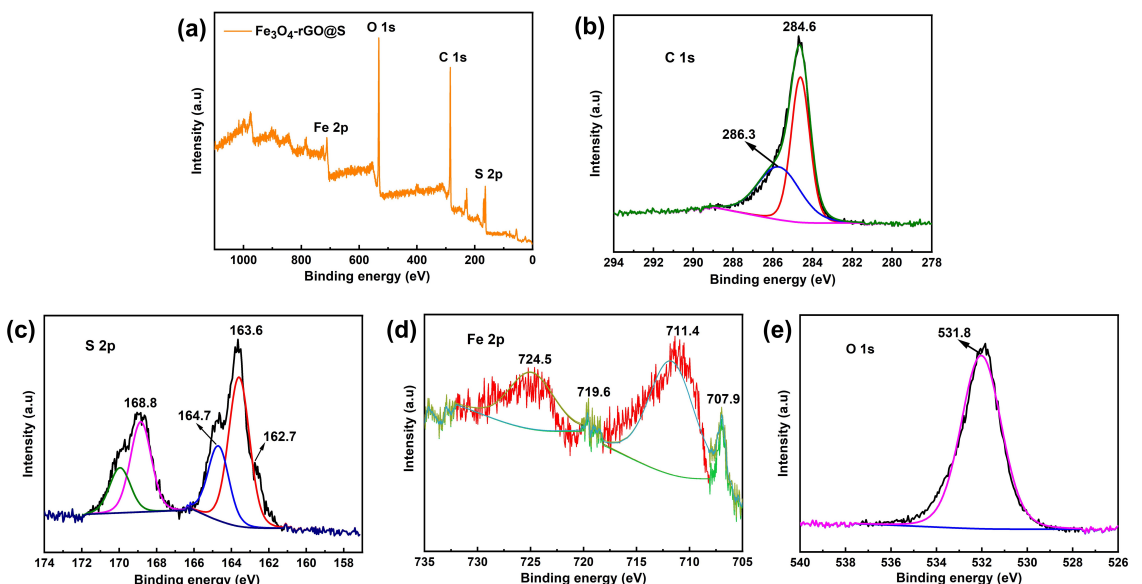


Figure 4. XPS analysis of the as-prepared Fe₃O₄-rGO@S. (a) survey spectrum; (b) C 1s region (c) S 2p region; (d) Fe 2p region and (e) O 1s region.

2.1. LPS Adsorption, Catalytic Conversion, and Li₂S Deposition on Functional Electrodes

The static adsorption test was conducted to study the chemical interaction and adsorption ability of Fe₃O₄ and Fe₃O₄-rGO samples. A small amount of Fe₃O₄ and Fe₃O₄-rGO was added to diluted solutions of Li₂S₆ and allowed to rest for 10 h and visually compared to observe the polysulfide-trapping and examine the color variation as compared to blank Li₂S₆ solution with time. Figure 5 (a) shows the digital image of a blank Li₂S₆ solution with Fe₃O₄-rGO and Fe₃O₄. The Fe₃O₄-rGO solution changes color from yellow to canary yellow and becomes transparent; in contrast, the Fe₃O₄ solution changes to slightly yellow to less transparent, and the blank Li₂S₆ solution remains pale yellowish. To understand further, a UV-vis spectrometer analysis was carried out for the supernatant of the Li₂S₆ solution from the Fe₃O₄ and Fe₃O₄-rGO samples; the blank Li₂S₆ solution was also tested for a comparison. The adsorption of blank Li₂S₆ indicates a peak at 290 nm (S₆²⁻).^[42] Compared to the blank Li₂S₆ solution, both Fe₃O₄-rGO and Fe₃O₄ exhibited weak absorption, as shown in Figure 5 (a), with Fe₃O₄-rGO showing the lowest absorption. The results demonstrated the polar nature of Fe₃O₄-rGO, which adsorbs polysulfide strongly and shows good

trapping ability. To gain more insight into the electrocatalytic activity of Fe₃O₄-rGO and Fe₃O₄ nanoparticles towards the kinetic conversion of the polysulfide redox reaction, symmetric cells were assembled with Fe₃O₄-rGO and Fe₃O₄ as working and counter electrodes both in the presence and absence of Li₂S₆ as the electrolyte. The cyclic voltammetry test was carried out across a potential range of -1 to 1 V, with a scan rate of 3 mV s⁻¹. The CV profile without the Li₂S₆ electrolyte shows the minor current response with capacitive behavior shown in the dotted line. However, the Li₂S₆ electrolyte exhibits a higher current response, implying the current response is primarily influenced by the polysulfide redox reaction, as opposed to double-layer capacitance. The CV curve of the Fe₃O₄-rGO electrode shows the highest current response compared to the Fe₃O₄ particle and distinct oxidation and reduction peaks, as shown in Figure 5 (b).^[30] The capability to anchor LPS molecules and lower electronic conductivity of Fe₃O₄ than Fe₃O₄-rGO significantly restricts the electron transfer from the confined LPS to the conductive network and delivers a lower current response during the conversion. The complete conversion reaction from Li₂S₄ to Li₂S can account for approximately 75% of the total theoretical capacity of sulfur. However, the insulating nature of Li₂S poses two major challenges: sluggish

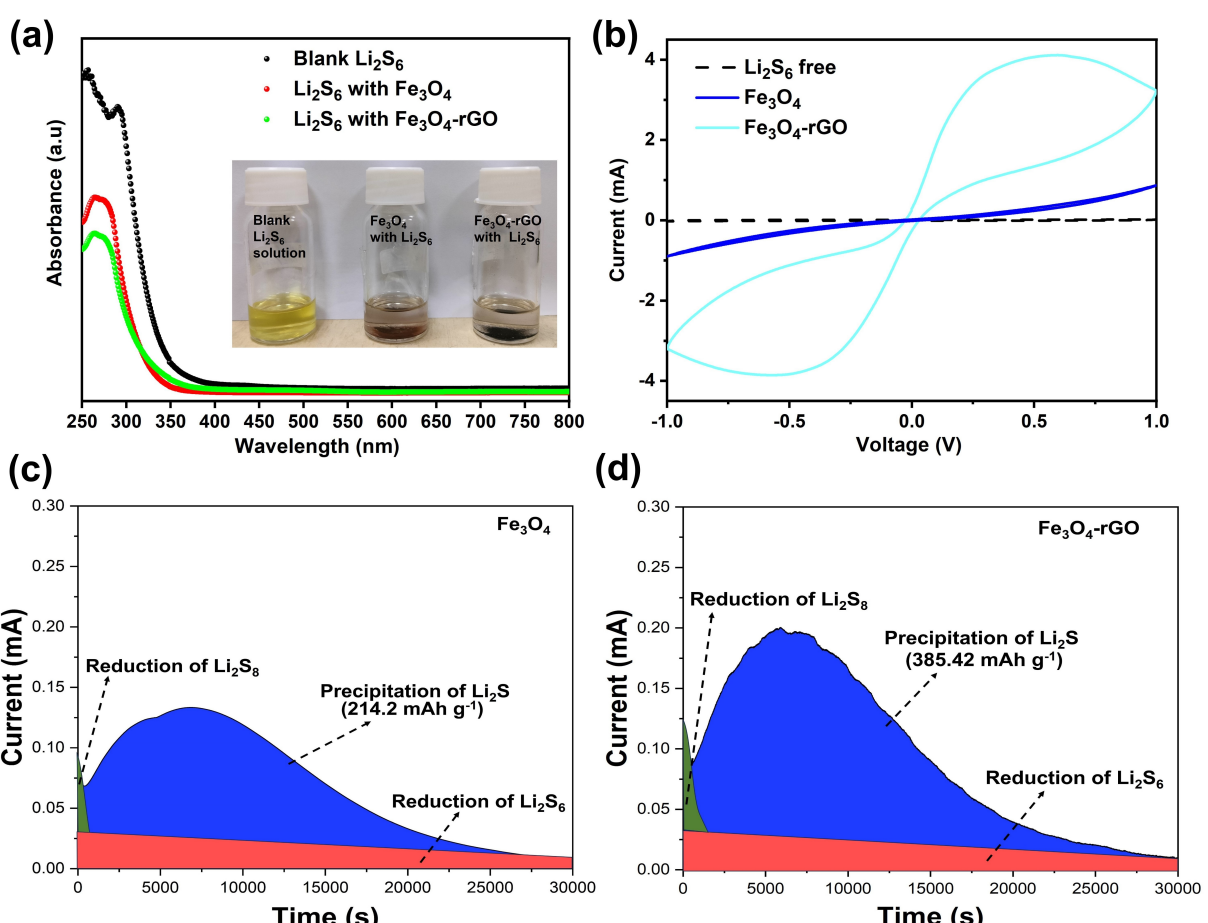


Figure 5. (a) UV-vis spectra of reference blank Li₂S₆ solution, Fe₃O₄ and Fe₃O₄-rGO with digital photograph of respective samples; (b) CV profiles of symmetric cells assembled with Fe₃O₄-rGO and Fe₃O₄ electrodes at 3 mV s⁻¹. Potentiostatic discharge curves of Li₂S deposition on the (c) Fe₃O₄ and; (d) Fe₃O₄-rGO electrodes.

reaction kinetics during the conversion of LPSs to Li_2S and electrode passivation, both of which result in inferior electrochemical performance. Therefore, regulating the deposition of Li_2S is essential for improving the capacity and rate capability of the LSBs.^[43,44] To evaluate the functionality of Fe_3O_4 -rGO and Fe_3O_4 cathode, a potentiostatic Li_2S deposition test was conducted. The coin cells were discharged potentiostatically at 2.05 V to initiate Li_2S deposition and nucleation. The calculated capacities for Li_2S deposition were 385.42 mAh g^{-1} for Fe_3O_4 -rGO and 214.2 mAh g^{-1} for Fe_3O_4 as shown in Figure 5 (c, d), indicating that Fe_3O_4 -rGO exhibits higher capacity. This suggests improved conversion kinetics for Fe_3O_4 -rGO compared to Fe_3O_4 .

2.2. Electrochemical Studies for Li-S Cells

To evaluate the performance of CR2032 coin cells, three distinct configurations were assembled, as shown in Figure 6 with (i) Fe_3O_4 -rGO@S, (ii) Fe_3O_4 -rGO@S_ Fe_3O_4 , and (iii) Fe_3O_4 -rGO@S_ Fe_3O_4 -rGO cathodes.

The initial charge-discharge curves of all three configurations are shown in Figure 7 (a) at 0.1 C. The respective discharge-specific capacities are 852, 1132, and 1258 mAh g^{-1} , showing that Fe_3O_4 -rGO@S exhibits the lowest specific capacity. The incorporation of the Fe_3O_4 -rGO interlayer into the Fe_3O_4 -rGO@S cathode facilitates electron transport, blocks polysulfide efficiently, and improves the discharge capacities.^[45] The

cathodes rate performance was evaluated at different current rates ranging from 0.1 to 2 C, as shown in Figure 7 (b). The discharge-specific capacities of Fe_3O_4 -rGO@S_ Fe_3O_4 -rGO at 0.1, 0.2, 0.5, 1, and 2 C are 1258, 1162, 1047, 707, and 505 mAh g^{-1} , respectively. In contrast, Fe_3O_4 -rGO@S_ Fe_3O_4 demonstrates specific discharge capacities of 1132, 865, 720, 568, 392 mAh g^{-1} , whereas Fe_3O_4 -rGO@S electrode exhibits discharge specific capacities of 862, 748, 560, 179, 20 mAh g^{-1} at 0.1, 0.2, 0.5, 1, and 2 C, respectively. The Fe_3O_4 -rGO@S composite exhibits the lowest specific capacities at all tested current densities. In contrast, Fe_3O_4 -rGO@S_ Fe_3O_4 -rGO shows a significant increase in discharge-specific capacity compared to Fe_3O_4 -rGO@S_ Fe_3O_4 at all rates up to 2 C. The improvement in specific capacity and rate capability is likely due to the three-dimensional porous composite structure and the strong bonding between polar Fe_3O_4 and reduced graphene oxide.^[33] Upon reverting to 0.1 C, the Fe_3O_4 -rGO@S_ Fe_3O_4 -rGO cells restored more than 95% of their initial capacities, demonstrating a relatively stable internal structure of the electrode. The cyclic stability of Fe_3O_4 -rGO@S, Fe_3O_4 -rGO@S_ Fe_3O_4 , and Fe_3O_4 -rGO@S_ Fe_3O_4 -rGO cathodes was measured at 0.2 C rate for 200 cycles by a galvanostatic charge-discharge test. Figure 7 (c) shows that Fe_3O_4 -rGO@S exhibits the lowest initial discharge capacity among the cathodes and the highest fading rate of 0.280% per cycle. Additionally, Fe_3O_4 -rGO@S cathode coulombic efficiency also fluctuates between 99% and 64%, demonstrating that the activity is degraded throughout the cycle. The

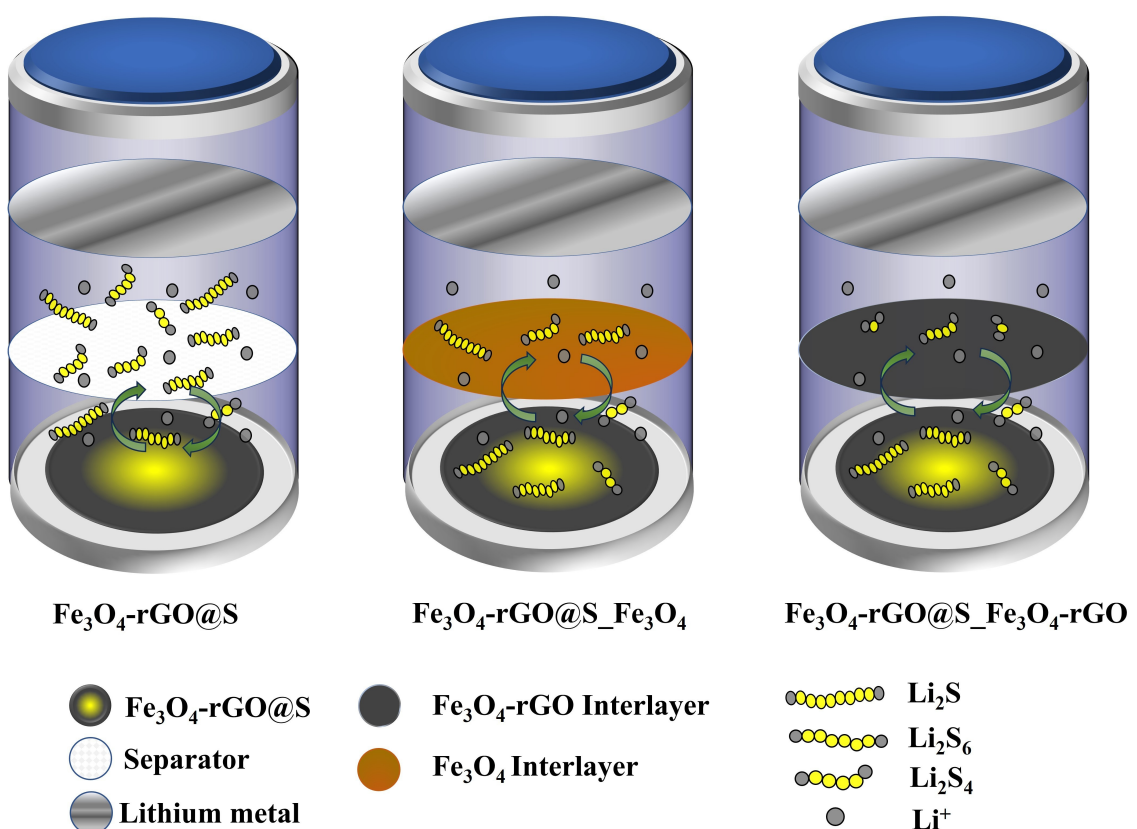


Figure 6. Schematic of CR2032 coin cell with three different configurations.

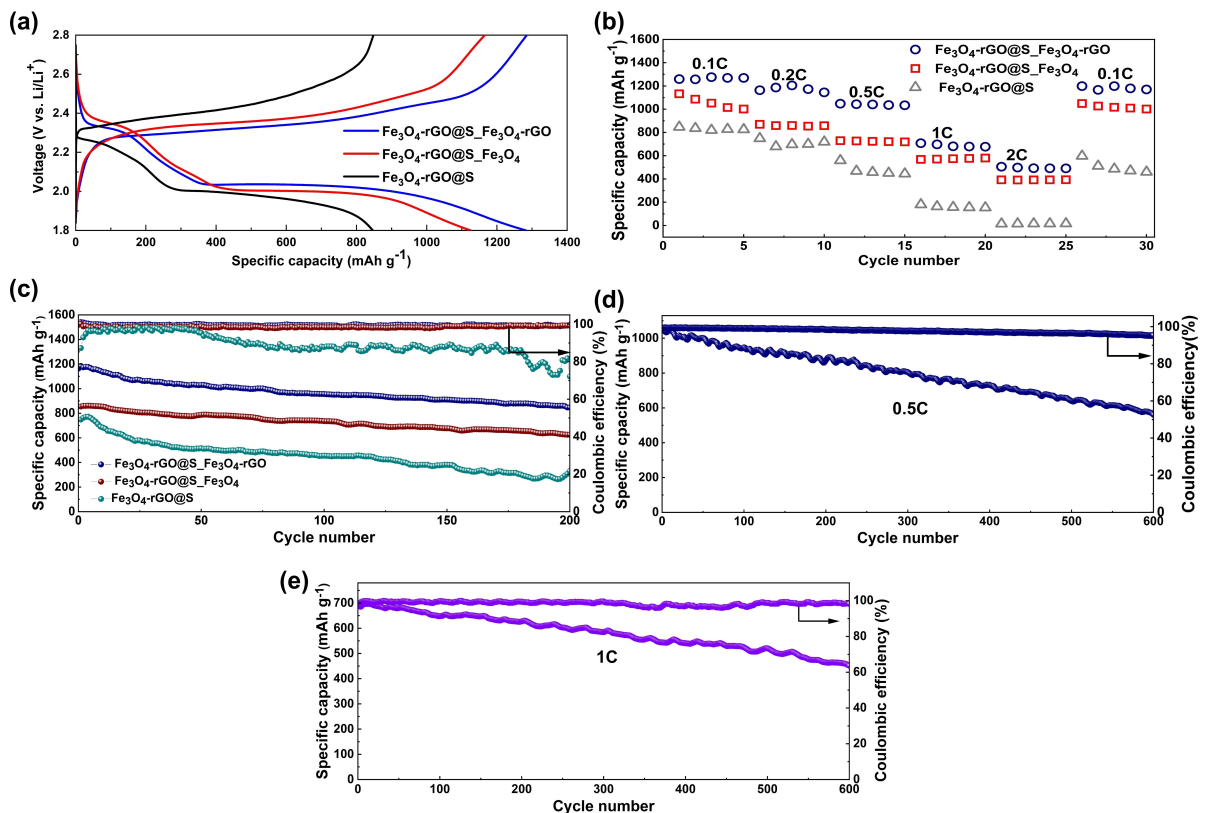


Figure 7. (a) Discharge-charge curves at 0.1 C; (b) rate performances; (c) cyclic stability of Fe₃O₄-rGO@S-Fe₃O₄-rGO, Fe₃O₄-rGO@S-Fe₃O₄ and Fe₃O₄-rGO@S cathode at 0.2 C rate; (d) cyclic stability of Fe₃O₄-rGO@S-Fe₃O₄-rGO cathode at 0.5 C and (e) at 1 C rate.

incorporation of the Fe₃O₄-rGO interlayer into the Fe₃O₄-rGO@S cathode led to an increase in the specific capacity, suggesting the effective inhibition of LPS shuttling. However, the specific capacity rapidly decreases as the number of charge-discharge cycles increases. This phenomenon is most likely caused by the sluggish redox kinetics of Fe₃O₄-rGO@S towards polysulfide shuttling. The Fe₃O₄-rGO@S-Fe₃O₄-rGO cathode shows the initial discharge capacity of 1162 mAh g⁻¹ at 0.2 C rate, the capacity fading rate is 0.13% per cycle, and the coulombic efficiency is close to 99%. On the other hand, the Fe₃O₄-rGO@S-Fe₃O₄ cathode exhibits a capacity fading of 0.1359% per cycle, and the coulombic efficiency is near 98%. The cyclic stability of the Fe₃O₄-rGO@S-Fe₃O₄-rGO cathode was evaluated at a 0.5 C rate for 600 cycles through galvanostatic charge-discharge testing. As shown in Figure 7 (d), the cyclic stability of Fe₃O₄-rGO@S-Fe₃O₄-rGO cathode at a 0.5 C rate shows a low capacity fading rate of 0.07% per cycle with a coulombic efficiency of ~99%. Conversely, the cyclic stability was also tested at a 1 C rate for 600 cycles. Figure 7 (e) shows the cyclic stability of Fe₃O₄-rGO@S-Fe₃O₄-rGO cathode at 1 C rate. Moreover, the Fe₃O₄-rGO@S-Fe₃O₄-rGO cathode shows the lowest fading rate of 0.059%, with coulombic efficiency close to ~99.2%. The results demonstrate that the Fe₃O₄-rGO interlayer exhibits excellent electrocatalytic activity toward the conversion and adsorption of polysulfide, which helps even more in preventing the shuttle effect and active material losses at high current density.

The CV curve of the Fe₃O₄-rGO@S-Fe₃O₄-rGO cathode in the voltage range of 1.8 to 2.8 V (vs. Li/Li⁺) with a scan rate of 0.1 mV s⁻¹ is shown in Figure 8 (a). The initial cathodic scan shows two reduction peaks at 2.35 and 2.02 V, corresponding to the conversion of elemental sulfur to long-chain soluble polysulfide (Li₂S_n, 4 ≤ n ≤ 8) and further reduction to short-chain insoluble polysulfide and finally to Li₂S. In the subsequent anodic scan, the sharp oxidation peak at 2.35 V corresponds to the reversible transition of Li₂S to polysulfide and further oxidation to elemental sulfur S₈. The CV implies that neither anodic nor cathodic peaks showed substantial changes, indicating better cyclic reversibility and reversible redox process.^[46] In order to explore the Li-ion diffusion coefficient of Fe₃O₄-rGO@S-Fe₃O₄-rGO, Fe₃O₄-rGO@S-Fe₃O₄ cathodes, the CVs were taken from 0.1 mV s⁻¹ to 0.4 mV s⁻¹ in the potential window of 1.8 to 2.8 V. Figure S4 (a, b) represents the CV profile of Fe₃O₄-rGO@S-Fe₃O₄-rGO, Fe₃O₄-rGO@S-Fe₃O₄ cathode at different scan rates. The peak current *I_p* increases with the scan rate *v*. The anodic peak I and cathodic peak (II and III) currents are graphically represented as a function of the scan rate *v* in Figure S4 (c, d). All the anodic and cathodic peak currents are linear with the square root of the scan rate. The linear relationship indicates a diffusion-limited electrochemical process where the Li-ion diffusion coefficient is directly correlated with the slope. The diffusion coefficient of Li-ion is calculated for the anodic peak and cathodic peak using the classical Randles-Sevcik equation.^[47]

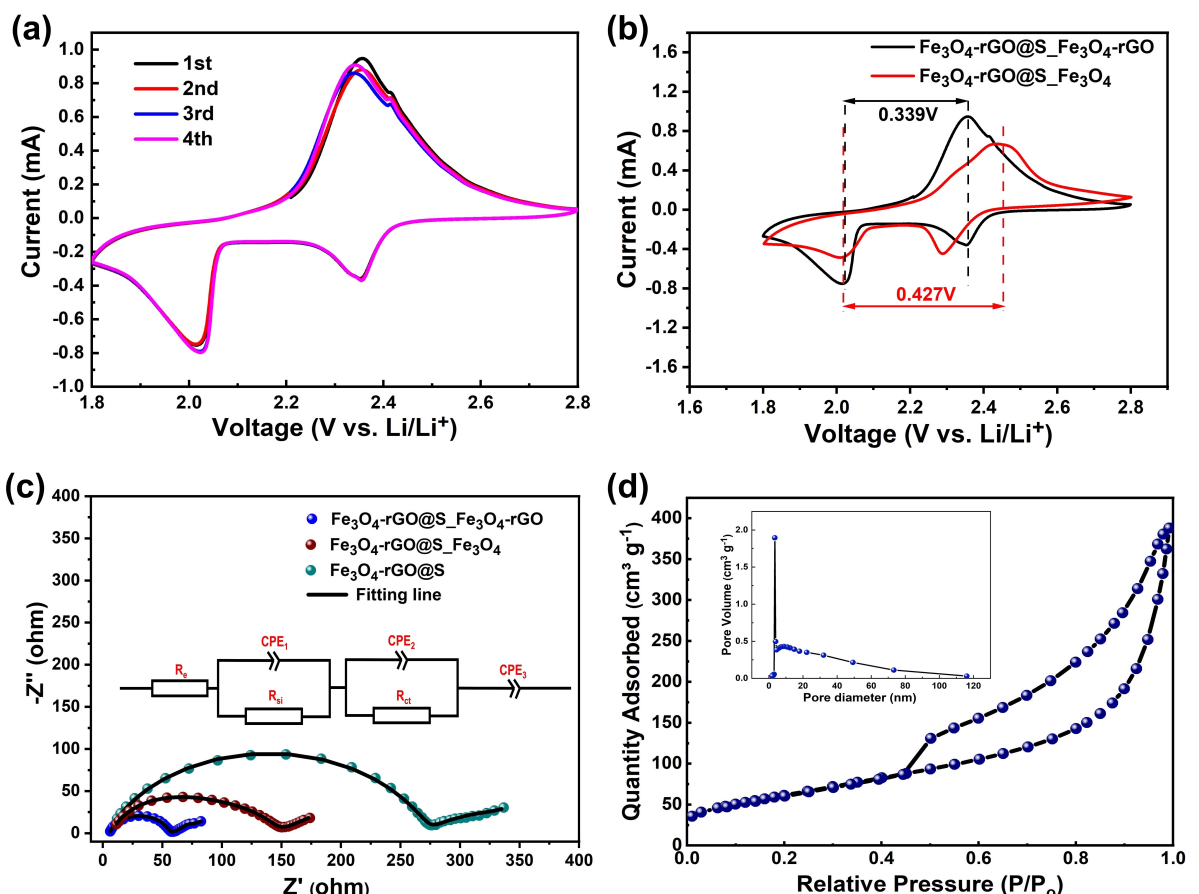


Figure 8. (a) CV curves of the $\text{Fe}_3\text{O}_4\text{-rGO}@S\text{-}\text{Fe}_3\text{O}_4\text{-rGO}$ cathode at 0.1 mVs^{-1} ; (b) CV curves of $\text{Fe}_3\text{O}_4\text{-rGO}@S\text{-}\text{Fe}_3\text{O}_4\text{-rGO}$ and $\text{Fe}_3\text{O}_4\text{-rGO}@S\text{-}\text{Fe}_3\text{O}_4$ cathodes at a scan rate of 0.1 mVs^{-1} ; (c) EIS of $\text{Fe}_3\text{O}_4\text{-rGO}@S\text{-}\text{Fe}_3\text{O}_4\text{-rGO}$, $\text{Fe}_3\text{O}_4\text{-rGO}@S\text{-}\text{Fe}_3\text{O}_4$ and $\text{Fe}_3\text{O}_4\text{-rGO}@S$ cathodes, and equivalent circuit; (d) Nitrogen adsorption-desorption isotherms with pore volume versus pore diameter plot of $\text{Fe}_3\text{O}_4\text{-rGO}$.

$$I_p = 2.69 * 10^5 * D^{0.5} * A * C * n^{1.5} * v^{0.5} \quad (1)$$

Where I_p is the peak current expressed in Ampere (A), A is the active electrode area (here 1.13 cm^2), D is the diffusion coefficient of Li-ion (cm^2/s), C is the concentration of the electrolyte (mol/ml), n is the number of electrons transferred in the redox process (here 2) and v is the scan rate (V/s).

The calculated diffusion coefficient for the cathodes is listed in Table 1. The measured diffusion coefficient of Li-ion of $\text{Fe}_3\text{O}_4\text{-rGO}@S\text{-}\text{Fe}_3\text{O}_4\text{-rGO}$ cathode is higher than that of $\text{Fe}_3\text{O}_4\text{-rGO}@S\text{-}\text{Fe}_3\text{O}_4$ cathode. This further signifies that the addition of the $\text{Fe}_3\text{O}_4\text{-rGO}$ interlayer to the $\text{Fe}_3\text{O}_4\text{-rGO}@S$ cathode enhances the diffusion kinetics. Furthermore, $\text{Fe}_3\text{O}_4\text{-rGO}@S\text{-}\text{Fe}_3\text{O}_4\text{-rGO}$ demonstrates the highest Li-ion diffusion coefficient across the redox peaks, which is attributed to the improved Li-ion trans-

port within the electrode diffusion and the kinetics of the sulfur redox reaction. This leads to enhanced specific capacity, cyclic stability, and rate performance. Furthermore, to provide a comprehensive comparison, the CV of $\text{Fe}_3\text{O}_4\text{-rGO}@S\text{-}\text{Fe}_3\text{O}_4\text{-rGO}$ and $\text{Fe}_3\text{O}_4\text{-rGO}@S\text{-}\text{Fe}_3\text{O}_4$ cathodes were combined at 0.1 mVs^{-1} . In comparison to $\text{Fe}_3\text{O}_4\text{-rGO}@S\text{-}\text{Fe}_3\text{O}_4$ cathode, the CV curves of $\text{Fe}_3\text{O}_4\text{-rGO}@S\text{-}\text{Fe}_3\text{O}_4\text{-rGO}$ cathode demonstrate an increase in current response and reduce in overpotential (0.339 V) between the cathodic and anodic peak than of $\text{Fe}_3\text{O}_4\text{-rGO}@S\text{-}\text{Fe}_3\text{O}_4$ (0.427 V) cathode as shown in Figure 8 (b). Incorporating the $\text{Fe}_3\text{O}_4\text{-rGO}$ interlayer is believed to boost the electrochemical reaction kinetics during the cyclic process by providing significant blocking and adhesion effects with polysulfide, consequently boosting the utilization efficiency of active material.

Table 1. The Li-ion diffusion coefficient of $\text{Fe}_3\text{O}_4\text{-rGO}@S\text{-}\text{Fe}_3\text{O}_4\text{-rGO}$ and $\text{Fe}_3\text{O}_4\text{-rGO}@S\text{-}\text{Fe}_3\text{O}_4$ cathodes.

Cathode	Diffusion coefficient ($\text{cm}^2 \text{ s}^{-1}$)	
	Peak I	Peak II
$\text{Fe}_3\text{O}_4\text{-rGO}@S\text{-}\text{Fe}_3\text{O}_4\text{-rGO}$	13.16×10^{-9}	4.13×10^{-9}
$\text{Fe}_3\text{O}_4\text{-rGO}@S\text{-}\text{Fe}_3\text{O}_4$	2.97×10^{-9}	1.92×10^{-9}

To elucidate the electrochemical kinetics of the cells by utilizing different separators, Electrochemical impedance spectroscopy (EIS) was performed, and the resultant data are illustrated in Figure 8 (c). The Nyquist plots exhibit a depressed semicircle in the high-frequency (HF) and mid-frequency (MF) ranges, transitioning to an inclined line at a low-frequency zone. These features are modeled by the equivalent circuit, as depicted in Figure 8 (c). The R_e represents the ohmic resistance, which can be found by extrapolating the Nyquist plot at the X-axis to the infinitely large frequency domain. R_{si} represents the surface interphase contact resistance, and R_{ct} corresponds to charge-transfer resistance. The constant phase element (CPE) is used instead of the capacitor to simulate the nonideal behavior of the electrodes. The Warburg elements (W_o) are changed with CPE₃ in the low-frequency domain, which depicts the infinite-length Warburg element, and also shows the diffusion of ions within the cathode.^[48] Among the cathodes, the Fe₃O₄-rGO@S-Fe₃O₄-rGO exhibits the lowest R_{ct} (19.30 Ω) values than the Fe₃O₄-rGO@S-Fe₃O₄ and Fe₃O₄-rGO@S cathodes as listed in the Table 2. The Fe₃O₄-rGO interlayer promotes the conductivity of the cathode by functioning as an upper current collector. Furthermore, the rGO establishes a continuous conductive network that facilitates rapid electron transit. Meanwhile, the Fe₃O₄ nanoparticles provide active electrochemical sites, facilitating efficient charge transfer. This highlights the dual role of the Fe₃O₄-rGO interlayer in the immobilization of LPS. Furthermore, the Fe₃O₄-rGO@S-Fe₃O₄-rGO cathode shows the lowest R_{si} (49.29 Ω) values and this can be attributed to the formation of a stable SEI membrane during the cycling process. To investigate further, we analyzed the specific surface area and pore size distribution of the Fe₃O₄-rGO. The isotherm obtained from nitrogen adsorption-desorption of Fe₃O₄-rGO represents Langmuir type IV isotherm, as shown in Figure 8 (d). Furthermore, the adsorption and desorption isotherm of nitrogen in the samples shows a hysteresis loop at a relative pressure higher than 0.4, indicative of mesoporous characteristics. The specific surface area is 224 m² g⁻¹, and the average pore diameter is 3.5 nm, indicating the mesoporous characteristics. Therefore, mesoporous structure and high specific surface area provide high sulfur loading and more space to accommodate volume change, promoting the diffusion of lithium ions and electrolytes through the porous network, which can promote the electrochemical activity during lithium polysulfide redox reactions.^[49] Moreover, provides more space to accommodate volume change.

Electrochemical Impedance spectroscopy (EIS) is the technique usually used to measure the impedance in the absence of direct current (DC) in a steady or stationary state. In contrast to EIS, Dynamic Electrochemical Impedance Spectroscopy (DEIS)

measures impedance during active charge or discharge cycles by sweeping the potential with a finite DC voltage. This approach offers advantages over EIS, as it allows the battery's state to change only slightly during measurement, maintaining a quasi-stationary state. The corresponding impedance profile is acquired at each stage by applying an AC signal.^[50,51] By utilizing this method, it is crucial to comprehend the kinetics of electrochemical reactions in the charge and discharge processes. In Li-S batteries, several electrochemical, physicochemical, and chemical reactions that occur during the discharge and charge processes define the characteristics of the battery. The interfacial activities at the electrode and electrolyte are crucial to understand, because various reaction kinetics occur during the discharge and charge processes for the formation and conversion of higher to lower-order LPS and vice versa. The dissolved LPS changes the physicochemical characteristics, reducing conductivity and increasing the viscosity of the electrolyte.^[52] These changes significantly impact the electrochemical processes in lithium-sulfur cells during cycling.

To obtain a profound understanding, DEIS measurements are acquired for the Fe₃O₄-rGO@S-Fe₃O₄-rGO cathode at each potential during the charge-discharge process in the potential window of 1.8–2.8 V after CV. The DEIS profile for Fe₃O₄-rGO@S-Fe₃O₄-rGO cathode during the charge and discharge processes are represented in Figure 9 (a, b). The high and mid-frequency portions of every Nyquist plot are semicircles, followed by an inclined line in the low-frequency region. The equivalent circuit shown in Figure 8 (c) is used to fit all of the Nyquist plots.

During the beginning of the discharge process (2.8–2.5 V), the diffusion tail rises, starts falling from 2.4 to 2.0 V, and then rises again. This can be explained by the conversion of elemental sulfur to higher-order LPS and dissolution into the liquid electrolyte experienced from the highest shuttle. Below 2.1 V, the insoluble solid Li₂S₂/Li₂S will form on the cathode surface and could prevent the diffusion of Li⁺ ion, consequently raising the diffusion tail. Conversely, during the charging process, a similar type of DEIS profile with a low diffusion tail at 2.3 V can be correlated to the transformation of lower-order polysulfide to higher-order polysulfide. Previous research by Garapati et al. has also demonstrated similar kind of results.^[53]

R_e , R_{si} , and R_{ct} , as previously detailed in the EIS profile, representing the ohmic resistance, surface interphase contact resistance, and charge-transfer resistance, respectively. The resistance values are plotted against voltage for a discharge process, as shown in Figure 9 (c). The R_e values remain relatively stable throughout the discharge process. This effect can be attributed to the trapping ability of the Fe₃O₄-rGO interlayer and minimizing the dissolution of polysulfide. The R_{si} shows an increase in value during the beginning of discharge, potentially

Table 2. Fitting values of three cathode from the simulation of equivalent circuit.

Cathode	R_e (Ω)	R_{si} (Ω)	R_{ct} (Ω)
Fe ₃ O ₄ -rGO@S-Fe ₃ O ₄ -rGO	4.41	49.29	19.30
Fe ₃ O ₄ -rGO@S-Fe ₃ O ₄	4.95	71.33	54.05
Fe ₃ O ₄ -rGO@S	6.91	268.8	66.55

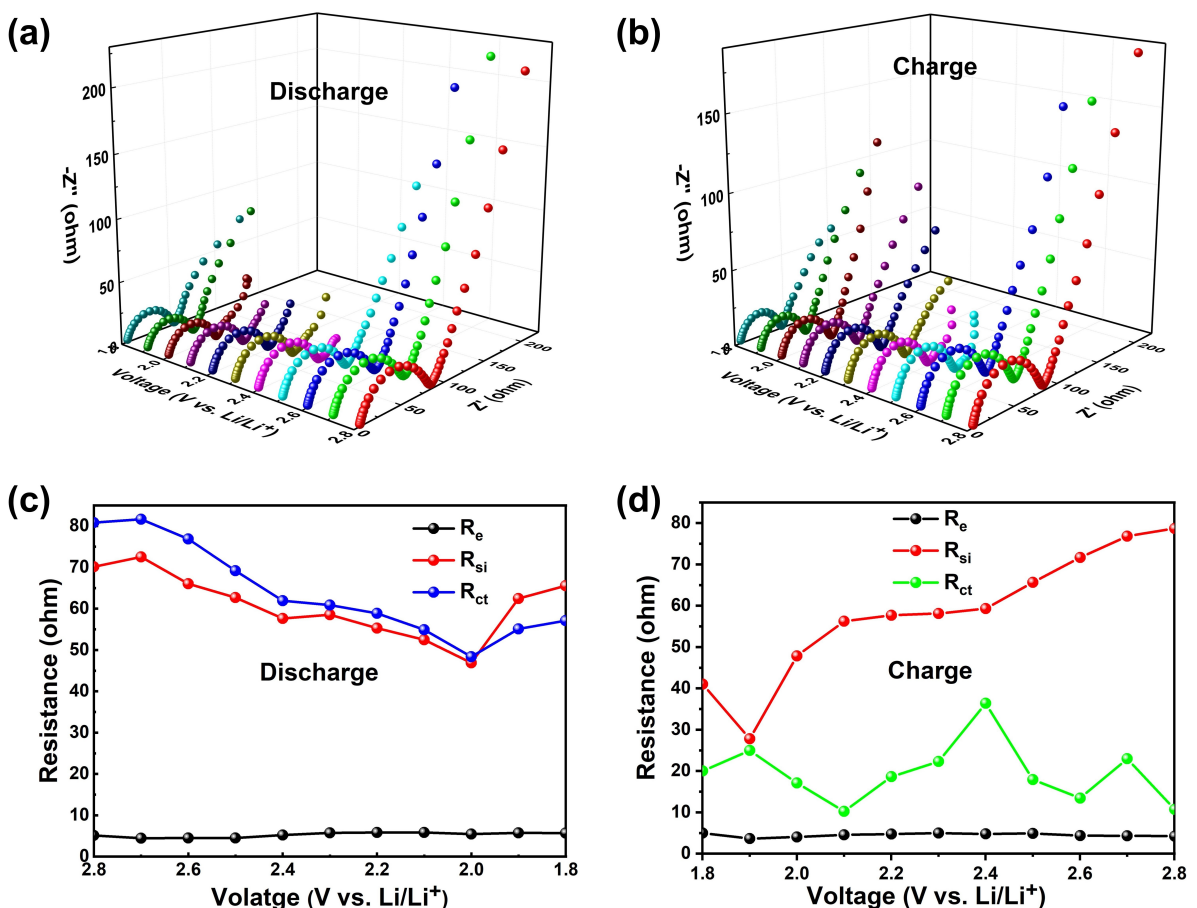


Figure 9. DEIS profiles of Fe_3O_4 -rGO@S- Fe_3O_4 -rGO cathode during discharge process (a), charge process (b), resistance versus voltage for discharge (c), and charge cycles(d).

arising from the reorganization of particles during the progression of the electrochemical reaction. Subsequently, there is a decrease in the R_{si} value as discharge proceeds due to sulfur reduction to LPS and rises again as a result of $\text{Li}_2\text{S}_2/\text{Li}_2\text{S}$ film formation.^[54] The R_{ct} value decreases during the beginning of the discharge; as the reaction progresses, the Fe_3O_4 -rGO facilitates electron transport and provides the conducting pathway of lithium-ion. Afterwards, the R_{ct} increases in value due to the generation and accumulation of $\text{Li}_2\text{S}/\text{Li}_2\text{S}_2$.

Similarly, for the charging process, resistance values are plotted against the charging voltage, and is shown in Figure 9 (d). R_e remains invariant during the charging process, analogous to its behavior during the discharge. As compared to the discharge process, the R_{si} and R_{ct} values exhibit distinct behavior, and R_{si} shows higher values than the R_{ct} values. At the beginning of the charge, Li_2S film starts to oxidize, resulting in a decrease in the value initially, and again starts increasing because of further oxidation to higher order polysulfide and the sulfur films. Indicating that the resistance of the electrolyte diffusing through the interlayer pores determines the R_{si} values, the electrochemical process during the charging of Li-S batteries is primarily governed by the transport properties of the electrolyte.^[48] The R_{si} increases at the beginning and

becomes minimum at 2.1 V, the phase transition of $\text{Li}_2\text{S}_2/\text{Li}_2\text{S}$ to higher-order polysulfides starts, increases with the formation of higher-order LPS, and finally decreases at the end of charging.

2.3. Post-Mortem Analysis

To further confirm the lithium polysulfide trapping capability of the Fe_3O_4 -rGO and Fe_3O_4 -coated separator facing toward the cathode side, the coin cells were dismantled inside the glove box after running 200 cycles at 0.2 C rate in the discharge state, and the separator was examined through SEM and Energy dispersive spectroscopy (EDS) (Figure S5). The top view image of the pristine Fe_3O_4 -rGO and Fe_3O_4 interlayer are shown in Figure S5 (a, b). The Figure S5 (a) represents the random arrangement of Fe_3O_4 decorated reduced graphene oxide before cycling, having good structural stability. The SEM with EDS mapping after cycling is shown in Figure S5 (c, d). After cycling, it was evident that many particles had been adsorbed on the Fe_3O_4 -rGO interlayer surface. Sulfur extends equally on the surface of the modified layer, as shown by the elemental mapping in the EDS analysis of the modified coating layer. This indicates that LPSs are obstructed by the Fe_3O_4 -rGO separator.

Furthermore, the high electrical conductivity of the Fe_3O_4 -rGO layer accelerates the movement of electrons and lithium ions, enabling the utilization of the active sulfur species that are absorbed on the coating layer. On the other hand, Fe_3O_4 shows randomly oriented agglomerated particles before cycling as depicted in Figure S5 (b). After cycling, Fe_3O_4 also adsorbs polysulfide because of its polar nature but it is less prominent than Fe_3O_4 -rGO, as represented in EDS elemental mapping of sulfur compared to Fe_3O_4 -rGO after cycling.

3. Conclusions

The functional Fe_3O_4 -rGO is prepared through a single-step pyrolysis method and employed as efficient sulfur host and electrocatalytic interlayer. The Fe_3O_4 -rGO as cathode benefits from having a high specific surface area, which can accommodate considerably high sulfur loading, and also provide ample space to buffer the volume expansion during lithiation. With the Fe_3O_4 -rGO interlayer, the kinetics of the redox process are promoted, and polysulfide shuttling is inhibited. The Li–S cells with Fe_3O_4 -rGO@S– Fe_3O_4 -rGO cathode exhibit initial capacity of 1258 mAh g⁻¹ at 0.1 C and maintaining 76% of its capacity after 400 cycle at 0.5 C. The CV and EIS results reveal that the Fe_3O_4 -rGO separator efficiently lowers the polarization voltage, thereby improving specific capacity and rate performance. The study also emphasizes the confinement of LPS on the Fe_3O_4 -rGO@S– Fe_3O_4 -rGO cathode and the interfacial redox kinetics studied by employing dynamic electrochemical impedance spectroscopy.

4. Supporting Information

Supporting information is available from online or from the author.

Acknowledgements

This research was conducted at Alternative Energy Nanotechnology laboratory (AENL), IIT Madras

Conflict of Interests

The authors declare no conflict of interest.

Data Availability Statement

The data that support the findings of this study are available from the corresponding author upon reasonable request.

Keywords: Lithium-sulfur batteries • Shuttle effects • High sulfur loading • Polysulfide inhibitor • Fe_3O_4 -rGO cathode

- [1] R. Fang, S. Zhao, Z. Sun, D. Wang, H. Cheng, F. Li, *Adv. Mater.* **2017**, *29*, 1606823.
- [2] A. Manthiram, Y. Fu, S. Chung, C. Zu, Y. Su, *Chem. Rev.* **2014**, *114*, 11751–11787.
- [3] X. Ji, L. F. Nazar, *J. Mater. Chem.* **2010**, *20*, 9821–9826.
- [4] P. G. Bruce, S. A. Freunberger, L. J. Hardwick, J. M. Tarascon, *Nat. Mater.* **2012**, *11*, 19–29.
- [5] X. Wang, G. Li, M. Li, R. Liu, H. Li, T. Li, M. Sun, Y. Deng, M. Feng, Z. Chen, *J. Energy Chem.* **2021**, *53*, 234–240.
- [6] L. Zhou, D. L. Danilov, F. Qiao, J. Wang, H. Li, R. A. Eichel, P. H. L. Notten, *Adv. Energy Mater.* **2022**, *12*, 2202094.
- [7] L. Zhang, H. Huang, H. Yin, Y. Xia, J. Luo, C. Liang, Y. Gan, X. Tao, W. Zhang, *J Mater Chem A Mater* **2015**, *3*, 16513–16519.
- [8] S. H. Chung, A. Manthiram, *Joule* **2018**, *2*, 710–724.
- [9] A. Hu, M. Zhou, T. Lei, Y. Hu, X. Du, C. Gong, C. Shu, J. Long, J. Zhu, W. Chen, X. Wang, J. Xiong, *Adv. Energy Mater.* **2020**, *10*, 1–26.
- [10] S. Huang, Z. Wang, Y. Von Lim, Y. Wang, Y. Li, D. Zhang, H. Y. Yang, *Adv. Energy Mater.* **2021**, *11*, 1–27.
- [11] S. O. Mirabootalebi, *Adv Compos Hybrid Mater* **2020**, *3*, 336–343.
- [12] M. J. Islam, M. J. Rahman, T. Mieno, *Adv Compos Hybrid Mater* **2020**, *3*, 285–293.
- [13] P. Xiao, F. Bu, G. Yang, Y. Zhang, Y. Xu, *Adv. Mater.* **2017**, *29*, 1–8.
- [14] J. Guo, Y. Xu, C. Wang, *Nano Lett.* **2011**, *11*, 4288–4294.
- [15] Y. Z. Zhang, Z. Zhang, S. Liu, G. R. Li, X. P. Gao, *ACS Appl. Mater. Interfaces* **2018**, *10*, 8749–8757.
- [16] H. Y. Zhou, Z. Y. Sui, S. Liu, H. Y. Wang, B. H. Han, *J. Colloid Interface Sci.* **2019**, *541*, 204–212.
- [17] Q. Zhu, H. Deng, Q. Su, G. Du, Y. Yu, S. Ma, B. Xu, *Electrochim. Acta* **2019**, *293*, 19–24.
- [18] G. Zheng, Y. Yang, J. J. Cha, S. S. Hong, Y. Cui, *Nano Lett.* **2011**, *11*, 4462–4467.
- [19] Z. Li, Y. Huang, L. Yuan, Z. Hao, Y. Huang, *Carbon N Y* **2015**, *92*, 41–63.
- [20] Z. Yin, S. Pan, Q. Cheng, G. Zhang, X. Yu, Z. Pan, H. Rao, X. Zhong, *J. Alloys Compd.* **2020**, *836*, 155341.
- [21] Z. Li, J. Zhang, B. Guan, D. Wang, L. M. Liu, X. W. Lou, *Nat. Commun.* **2016**, *7*, 1–11.
- [22] Z. Li, B. Y. Guan, J. Zhang, X. W. (David) Lou, *Joule* **2017**, *1*, 576–587.
- [23] J. Zhang, Y. Shi, Y. Ding, W. Zhang, G. Yu, *Nano Lett.* **2016**, *16*, 7276–7281.
- [24] X. Wang, G. Li, J. Li, Y. Zhang, A. Wook, A. Yu, Z. Chen, *Energy Environ. Sci.* **2016**, *9*, 2533–2538.
- [25] Z. Liu, X. Zheng, S. L. Luo, S. Q. Xu, N. Y. Yuan, J. N. Ding, *J. Mater. Chem. A* **2016**, *4*, 13395–13399.
- [26] Y. Zhang, L. Wang, A. Zhang, Y. Song, X. Li, H. Feng, X. Wu, P. Du, *Solid State Ionics* **2010**, *181*, 835–838.
- [27] X. Tao, J. Wang, Z. Ying, Q. Cai, G. Zheng, Y. Gan, H. Huang, Y. Xia, C. Liang, W. Zhang, Y. Cui, *Nano Lett.* **2014**, *14*, 5288–5294.
- [28] Z. Cui, C. Zu, W. Zhou, A. Manthiram, J. B. Goodenough, *Adv. Mater.* **2016**, *28*, 6926–6931.
- [29] Y. Song, W. Cai, L. Kong, J. Cai, Q. Zhang, J. Sun, *Adv. Energy Mater.* **2020**, *10*, 1–21.
- [30] M. Ding, S. Huang, Y. Wang, J. Hu, M. E. Pam, S. Fan, Y. Shi, Q. Ge, H. Y. Yang, *J. Mater. Chem. A* **2019**, *7*, 25078–25087.
- [31] J. He, L. Luo, Y. Chen, A. Manthiram, *Adv. Mater.* **2017**, *29*, 1–5.
- [32] K. Lu, H. Zhang, S. Gao, H. Ma, J. Chen, Y. Cheng, *Adv. Funct. Mater.* **2019**, *29*, 1–8.
- [33] Y. Liu, X. Qin, S. Zhang, G. Liang, F. Kang, G. Chen, B. Li, *ACS Appl. Mater. Interfaces* **2018**, *10*, 26264–26273.
- [34] A. Ghosh, D. Ganguly, R. Sundara, *J. Electroanal. Chem.* **2021**, *895*, 115386.
- [35] A. K. Das, S. Sahoo, P. Arunachalam, S. Zhang, J. J. Shim, *RSC Adv.* **2016**, *6*, 107057–107064.
- [36] J. Liu, K. Chen, Y. Zhang, L. Zhou, F. Wang, X. Xiang, H. Wu, *Prog. Org. Coat.* **2024**, *196*, 108677.
- [37] Z. Yao, L. Zhou, H. Yin, X. Wang, D. Xie, X. Xia, C. Gu, J. Tu, Z. J. Yao, L. M. Zhou, H. Y. Yin, X. L. Wang, X. H. Xia, C. D. Gu, J. P. Tu, D. Xie, *Small* **2019**, *15*, 1904433.
- [38] Z. Wang, Y. Dong, H. Li, Z. Zhao, H. Bin Wu, C. Hao, S. Liu, J. Qiu, X. W. D. Lou, *Nature Communications* **2014**, *5*, 1–8.
- [39] A. G. Schaufuß, H. W. Nesbitt, I. Kartio, K. Laajalehto, G. M. Bancroft, R. Szargan, *J. Electron Spectrosc. Relat. Phenom.* **1998**, *96*, 69–82.
- [40] L. Li, P. Ma, S. Hussain, L. Jia, D. Lin, X. Yin, Y. Lin, Z. Cheng, L. Wang, *Sustain. Energy Fuels* **2019**, *3*, 1749–1756.
- [41] H. Zhang, M. Zhang, R. Liu, T. He, L. Xiang, X. Wu, Z. Piao, Y. Jia, C. Zhang, H. Li, F. Xu, G. Zhou, Y. Mai, *Nat. Commun.* **2024**, *15*, 1–13.

- [42] S. Yao, R. Guo, F. Xie, Z. Wu, K. Gao, C. Zhang, X. Shen, T. Li, S. Qin, *Electrochim. Acta* **2020**, *337*, 135765.
- [43] Y. Zuo, Y. Zhu, R. Wan, W. Su, Y. Fan, R. Liu, Y. Tang, Y. Chen, *Chem. Eng. J.* **2021**, *415*, 129053.
- [44] Q. Lin, L. Huang, W. Liu, Z. Li, R. Fang, D. W. Wang, Q. H. Yang, W. Lv, *Phys. Chem. Chem. Phys.* **2021**, *23*, 21385–21398.
- [45] P. Cheng, P. Guo, D. Liu, Y. Wang, K. Sun, Y. Zhao, D. He, *J. Alloys Compd.* **2019**, *784*, 149–156.
- [46] M. Li, S. Ji, X. Ma, H. Wang, X. Wang, V. Linkov, R. Wang, *ACS Appl. Mater. Interfaces* **2022**, *14*, 16310–16319.
- [47] Z. Li, Y. Cong, J. Zhao, H. Su, Y. Shang, H. Liu, *ACS Appl. Electron. Mater.* **2024**, *6*, 3780–3789.
- [48] Z. Deng, Z. Zhang, Y. Lai, J. Liu, J. Li, Y. Liu, *J. Electrochem. Soc.* **2013**, *160*, A553–A558.
- [49] Q. Pang, D. Kundu, L. F. Nazar, *Mater. Horiz.* **2016**, *3*, 130–136.
- [50] J. Huang, Z. Li, J. Zhang, *J. Power Sources* **2015**, *273*, 1098–1102.
- [51] J. Huang, H. Ge, Z. Li, J. Zhang, *Electrochim. Acta* **2015**, *176*, 311–320.
- [52] V. S. Kolosnitsyn, E. V. Kuzmina, E. V. Karaseva, S. E. Mochalov, *J. Power Sources* **2011**, *196*, 1478–1482.
- [53] M. S. Garapati, R. Sundara, *Electrochim. Acta* **2020**, *362*, 137035.
- [54] N. A. Cañas, K. Hirose, B. Pascucci, N. Wagner, K. A. Friedrich, R. Hiesgen, *Electrochim. Acta* **2013**, *97*, 42–51.

Manuscript received: November 10, 2024

Revised manuscript received: January 11, 2025

Accepted manuscript online: January 17, 2025

Version of record online: January 28, 2025